nature nanotechnology

ARTICLES

https://doi.org/10.1038/s41565-021-00857-9

Check for updates

Covalently interconnected transition metal dichalcogenide networks via defect engineering for high-performance electronic devices

Stefano Ippolito[1], Adam G. Kelly[2], Rafael Furlan de Oliveira[1], Marc-Antoine Stoeckel[1], Daniel Iglesias[1], Ahin Roy[3], Clive Downing[3], Zan Bian[4], Lucia Lombardi[4], Yarjan Abdul Samad[4], Valeria Nicolosi[3], Andrea C. Ferrari[4], Jonathan N. Coleman[2] and Paolo Samorì[1]✉

Solution-processed semiconducting transition metal dichalcogenides are at the centre of an ever-increasing research effort in printed (opto)electronics. However, device performance is limited by structural defects resulting from the exfoliation process and poor inter-flake electronic connectivity. Here, we report a new molecular strategy to boost the electrical performance of transition metal dichalcogenide-based devices via the use of dithiolated conjugated molecules, to simultaneously heal sulfur vacancies in solution-processed transition metal disulfides and covalently bridge adjacent flakes, thereby promoting percolation pathways for the charge transport. We achieve a reproducible increase by one order of magnitude in field-effect mobility (μ_{FE}), current ratio (I_{ON}/I_{OFF}) and switching time (τ_S) for liquid-gated transistors, reaching 10^{-2} cm^2 V^{-1} s^{-1}, 10^4 and 18 ms, respectively. Our functionalization strategy is a universal route to simultaneously enhance the electronic connectivity in transition metal disulfide networks and tailor on demand their physicochemical properties according to the envisioned applications.

Solution-processed layered materials have a wide-ranging portfolio of physicochemical properties, whose inherent features make them prime candidates for low-cost and scalable applications in (opto)electronics, (photo)catalysis, (bio)sensing and biomedicine[1–4]. Much work has been done on the production and isolation of solution-processed semiconducting transition metal dichalcogenides (TMDs) by scalable methods[5–7]. Liquid-phase exfoliation (LPE) is the main route for preparing high-concentration and high-volume TMD dispersions[8,9], where bulk crystals are dispersed and exfoliated in a specific solvent via mechanical energy transfer that overcomes the van der Waals interactions within the layered structures. The high throughput achieved by LPE promotes the use of TMDs in many different applications, exploiting pristine or hybrid materials in the form of dispersions, coatings and thin-films produced by diverse deposition techniques, including inkjet printing, spray coating, roll-to-roll processing, dropcasting and so on[4,7,10,11].

Although LPE provides the best trade-off amongst cost, purity and yield[11,12], it has some limitations when the final application concerns (opto)electronics, where structural defects in the materials play a detrimental role[1,13]. One of the most widely employed LPE methods makes use of a tip horn sonicator that peels layered materials apart, thanks to vibrational and cavitation forces that arise from the generation and propagation of transverse waves within the solvent[14]. Consequently, the formation and implosion of cavitation bubbles generates energetic shock waves that induce localized temperature and pressure conditions that are sufficient to peel individual layers off the bulk structure, with a critical influence on their ultimate lateral size[15]. This energetic exfoliation procedure results in a mild formation of new defects and major propagation of inherent bulk defects in the exfoliated layers. As suggested by thermodynamic considerations, zero-dimensional defects are the most abundant stoichiometric deficiencies in TMDs, especially chalcogen vacancies mainly located at the flake edges and whose formation energy is a few eV (~2 eV in the case of sulfur vacancies)[16,17]. These structural defects strongly affect the electronic properties of solution-processed TMDs, with detrimental effects on the electrical performance of related devices[18,19].

Many groups have developed molecular strategies for tuning the physicochemical properties of solution-processed TMDs and overcoming the aforementioned limitations, enlarging their range of applicability in electronics and optoelectronics[20–22]. In the case of electrical devices based on individual flakes, a promising strategy exploits thiolated molecular systems to heal sulfur vacancies in transition metal disulfides (MS_2), thereby restoring the pristine crystal structure of the material and enhancing its electrical properties[23,24]. Nevertheless, in thin-film TMD-based devices, an additional and limiting factor related to inter-flake electrical resistance emerges, resulting in a significant hindrance of charge-carrier transport[25,26]. This represents a major bottleneck in the development of solution-processed TMD-based optoelectronics, especially in large-area and high-performance device applications.

Here, we report a molecular strategy to simultaneously heal sulfur vacancies in solution-processed MS_2 (M = Mo, W and Re) and increase the inter-flake electronic connectivity by means of dithiolated molecular systems. Using π-conjugated dithiolated molecules (HS–R–SH), we prove via diverse multiscale analysis the simultaneous: (1) healing of sulfur vacancies to restore the MS_2 crystal structure and decrease the related stoichiometric deficiencies acting as charge-scattering centres and (2) covalent bridging of adjacent

[1]Université de Strasbourg, CNRS, ISIS UMR 7006, Strasbourg, France. [2]School of Physics, Centre for Research on Adaptive Nanostructures and Nanodevices (CRANN) and Advanced Materials and Bioengineering Research (AMBER), Trinity College Dublin, Dublin, Ireland. [3]School of Chemistry, Centre for Research on Adaptive Nanostructures and Nanodevices (CRANN) and Advanced Materials and Bioengineering Research (AMBER), Trinity College Dublin, Dublin, Ireland. [4]Cambridge Graphene Centre, Cambridge University, Cambridge, United Kingdom. ✉e-mail: samori@unistra.fr

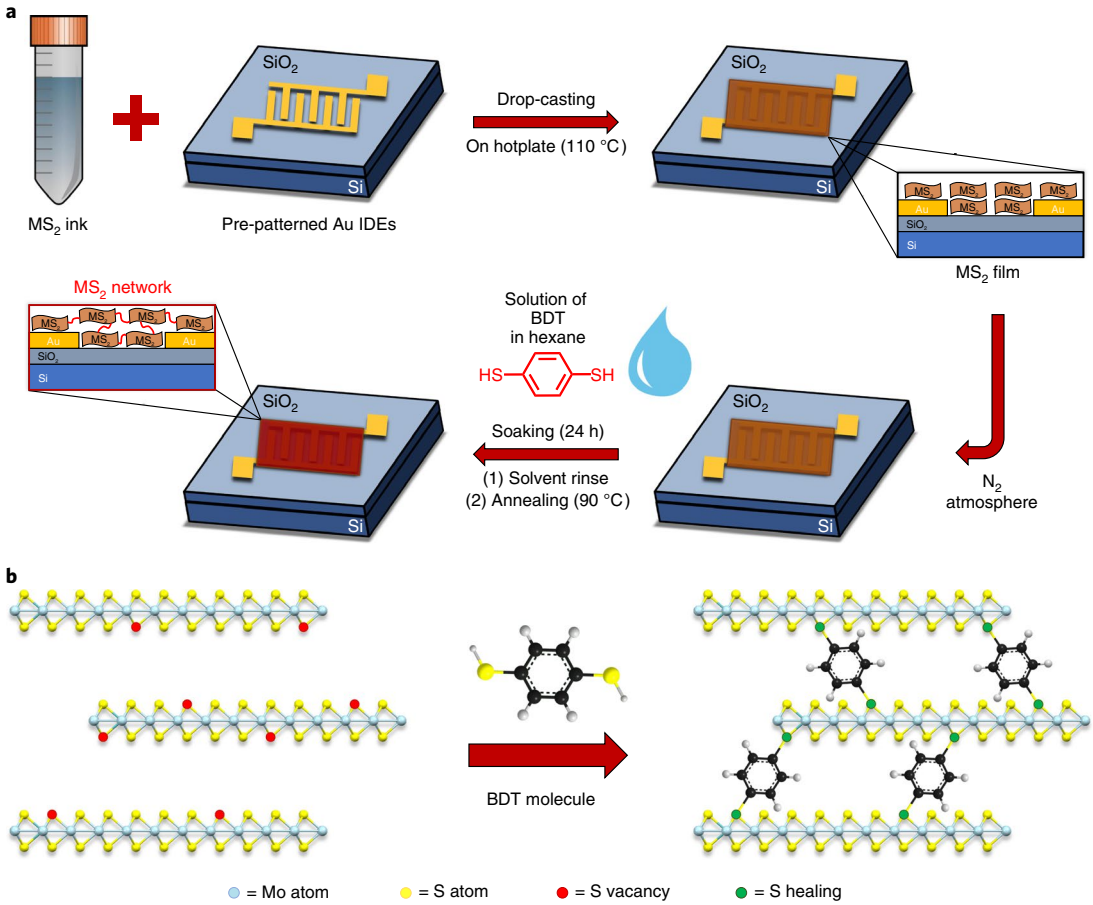

Fig. 1 | Functionalization strategy for production of covalently interconnected MS_2 networks. a, Schematic of ink deposition and in situ functionalization to produce MS_2 networks via BDT treatment. **b**, Schematic of sulfur-vacancy healing mechanism in MoS_2 films by means of dithiolated molecules and related inter-flake networking.

flakes, resulting in an enhanced charge-carrier transport through an interconnected network. We capitalize on the in situ functionalization approach of TMDs, exposing the inorganic materials to molecular linkers just after their deposition on a substrate. This is crucial for the formation of long-range pathways that exhibit superior charge-transport characteristics, likewise the bridging of disordered regions in conjugated polymer chains[27].

Our approach is an innovative and universal functionalization method, capable of improving the performance of devices based on solution-processed MS_2 for large-area electronic applications. We apply this strategy in liquid-gated thin-film transistors (LG-TFTs) fabricated by dropcasting MS_2 dispersions on SiO_2/Si substrates pre-patterned with gold interdigitated electrodes (IDEs), followed by exposure to aromatic and conjugated 1,4-benzenedithiol (BDT) molecules. This boosts the characteristics of MS_2-based LG-TFTs by one order of magnitude, leading to state-of-the-art electrical performance in terms of field-effect mobilities (μ_{FE}) and I_{ON}/I_{OFF}, along with the fastest switching speed reported so far for devices of this kind[28]. Improved water stability and mechanical robustness are other unique features exhibited by the covalently bridged MS_2 networks.

Device fabrication and in situ functionalization

MS_2 colloidal dispersions (inks), where M = Mo, W and Re, are produced and characterized prior to their use in devices (see Supplementary Sections 1 and 2, Extended Data Fig. 1). MS_2 inks are then dropcast on SiO_2/Si substrates with 2.5-μm-spaced gold IDEs for TFT measurements. The ink deposition is performed on substrates placed onto a 110 °C heated hotplate to assist solvent (2-propanol) evaporation and elimination of humidity traces during casting (Fig. 1a). Morphological characterizations (scanning electron microscopy and atomic force microscopy) of the deposited materials show a large-scale (micrometre) uniform coverage of the electrodes (important to enable charge-percolation pathways), a thickness of ~700 ± 100 nm and an average root-mean-squared roughness, $R_{r.m.s.} \approx 95 \pm 10$ nm over a 25 μm² area (Supplementary Fig. 3a).

In our work, MS_2 networks are formed by bridging adjacent flakes and taking advantage of the higher defect density at the edge sites with respect to basal planes, as confirmed by high-angle annular dark-field scanning transmission electron microscopy (HAADF-STEM) investigation (Supplementary Fig. 2, Extended Data Fig. 2). More specifically, the MS_2 thin-films are functionalized in a nitrogen-filled glovebox using a 50 mM saturated solution of BDT in anhydrous hexane to promote the formation of covalently linked MS_2 networks. The whole preparation of the BDT solution (weighing of powder and dissolution) is carried out under a nitrogen atmosphere to avoid thiol oxidation reactions induced by impurities[29]. The coated slides are soaked in BDT solution at room temperature for 24 h inside a sealed container, followed by rinsing in hexane and annealing on a hotplate at 90 °C for 30 min. No remarkable morphological variations are detected after thiol exposure and the network features remain similar to those of pristine films (Supplementary Fig. 3b). The functionalization process is designed to simultaneously heal sulfur vacancies in MS_2 films and covalently bridge adjacent flakes, thereby promoting their modification at the molecular level (Fig. 1b).

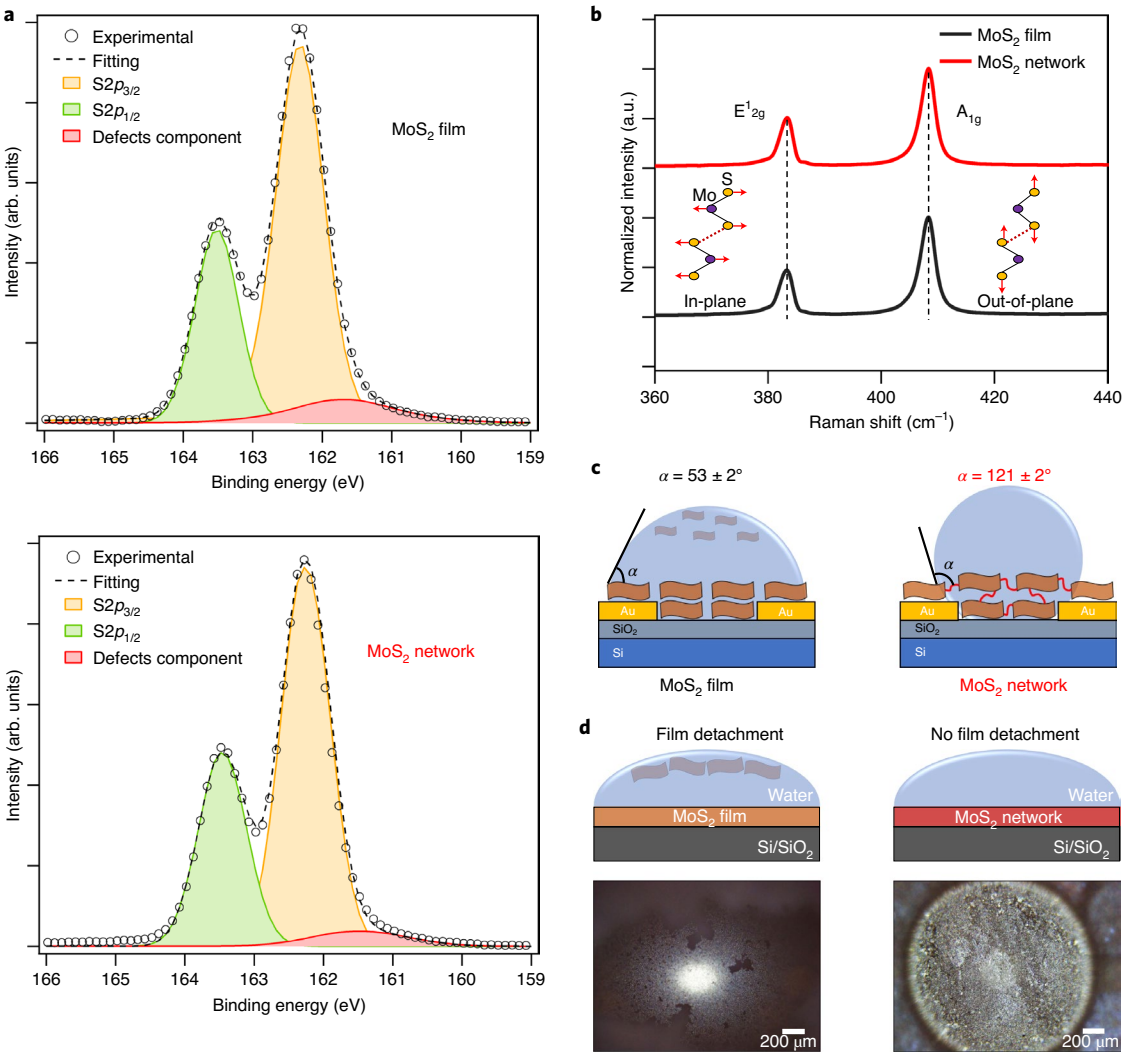

Fig. 2 | Characterization of MS_2 films and networks. a, High-resolution S2*p* XPS spectra for MoS_2 film (top) and network (bottom). arb. units, arbitrary units. **b**, Raman spectra of MoS_2 film (black) and network (red), highlighting the two main E^1_{2g} and A_{1g} peaks related to in-plane and out-of-plane vibrations, respectively. **c**, Schematic of WCA results for MoS_2 film (left) and network (right). **d**, Schematics (top) and optical images (bottom) showing the different water stability of the MoS_2 film (left) and network (right).

Multiscale characterization of MS_2 networks

We assess the effects of in situ functionalization with BDT molecules by independent multiscale techniques. X-ray photoelectron spectroscopy (XPS) measurements provide evidence for MS_2 chemical functionalization, as illustrated in Fig. 2a by the S2*p* high-resolution spectra of dropcast solution-processed MoS_2 before (as a film) and after (as a network) BDT treatment. The MoS_2 S2*p* spectrum displays two main peaks at ~162.3 and ~163.5 eV, assigned to the $S2p_{3/2}$ and $S2p_{1/2}$ components[30], respectively. An additional component can be deconvoluted at ~161.5 eV and ascribed to defects, for example, a vacancy neighbouring a sulfur atom[30,31]. Such a minority component at lower binding energies is due to the charge localized on sulfur that, once sulfur has been desorbed, can be redistributed on the first neighbouring atoms, enhancing Coulomb screening[30]. The substoichiometric MoS_{2-x} component at ~161.5 eV is related to unsaturated sulfur ligands[31], such as sulfur vacancies, and decreases from 8.0 ± 0.5% to 5.0 ± 0.5% upon BDT treatment, proving how the exposure to thiolated molecules leads to a decrease of chalcogen vacancy defects in solution-processed MoS_2. Since different sulfur ligands have minimal differences in binding energies, their identification in XPS spectra is not always straightforward and most literature reports focus on just MoS_2 (see Supplementary Section 4 for further information on XPS data analysis, Extended Data Fig. 3).

The Raman spectra of MoS_2 pristine films and networks (Fig. 2b) show no major differences, suggesting that the functionalization process does not damage the flakes. The full width at half maximum of both E^1_{2g} and A_{1g} peaks narrows by ~10% upon thiol exposure, combined with a small blue shift and an increase of the E^1_{2g}/A_{1g} intensity ratio (see Supplementary Section 5). This is consistent with a reduction in defect density and suppression of defect-activated modes[32,33], endorsing the healing of sulfur vacancies by thiolated molecules. A statistical Raman analysis of MoS_2 films and networks is provided in Supplementary Section 5.

Evidence of network formation comes from the distinctive characteristics and macroscopic properties of BDT-treated MS_2 samples. Pristine MoS_2 films on electrode-free SiO_2/Si substrates show hydrophilic behaviour, with an average static water contact angle (WCA), α, of 53 ± 2° in agreement with literature[34], whereas small fluctuations around these numbers depend on the material growth, exfoliation and deposition technique[35]. Upon functionalization, the MoS_2 networks show strong hydrophobic behaviour characterized by an average α of 121 ± 2° (Fig. 2c), where the

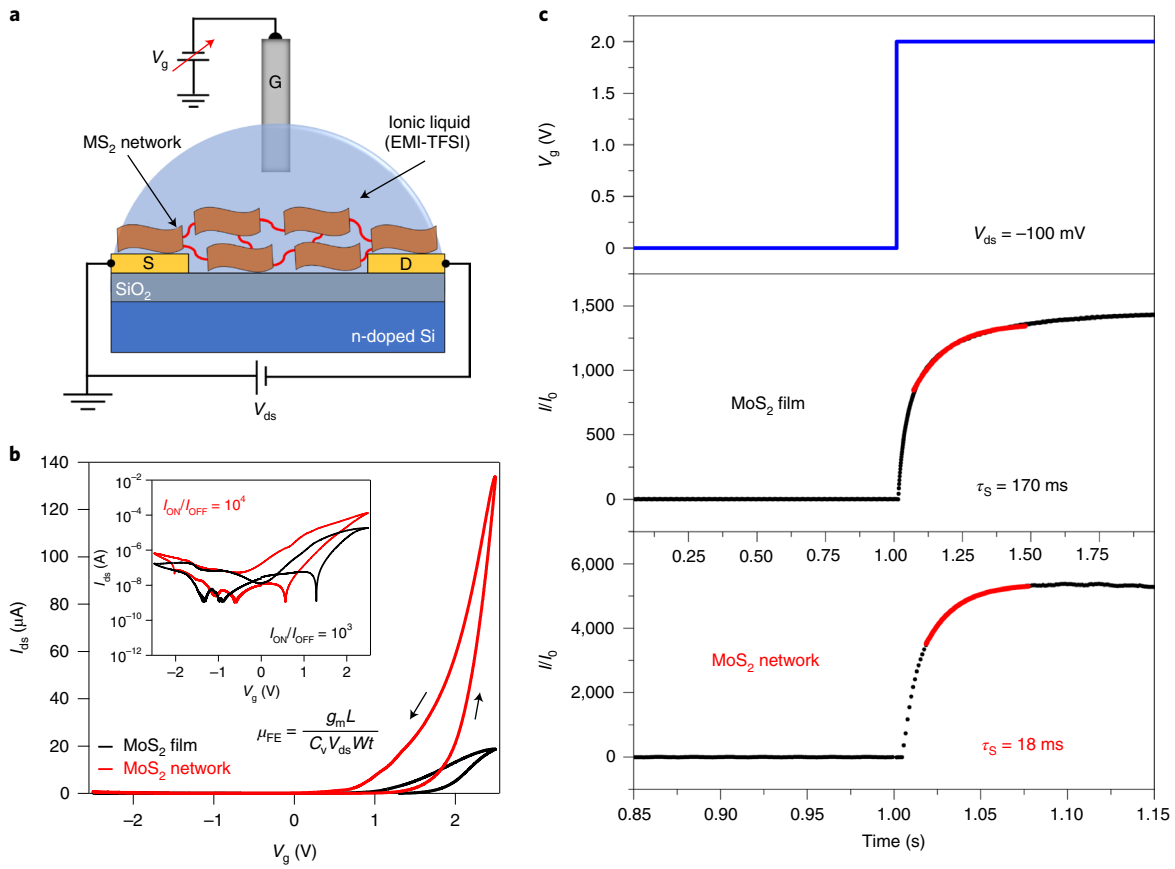

Fig. 3 | Electrical properties of LG-TFTs based on MoS_2 films and networks. a, LG-TFT geometry. S, source; D, drain; G, gate; V_{ds}, source–drain voltage. **b**, Transfer curves for MoS_2 films and networks with $V_{ds} = -100$ mV and V_g sweeping from −2.5 to +2.5 V. Inset shows the log-scale current characteristics and the equation for calculation of μ_{FE}. g_m, transconductance; L, channel length; C_v, volumetric capacitance; W, channel width; t, film/network thickness. **c**, LG-TFT switching characteristics under V_g step and corresponding time-dependent normalized current response (I/I_0). The red line delimits the range in which a non-linear fitting can be used to extrapolate τ_S.

Table 1 | Main figures of merit for electrical devices based on MoS_2 films and networks

Figure of merit	MoS_2 film	MoS_2 network
$\mu_{FE}/\mu_{FE,\ film}$	1	10 ± 1
I_{ON}/I_{OFF}	10^3	10^4
V_{TH}(V)	1.9 ± 0.1	1.8 ± 0.1
τ_S(ms)	170 ± 5	18 ± 2

Upon exposure to BDT and network formation, LG-TFTs exhibit a reproducible enhancement of one order of magnitude in the main device figures of merit, with minimal changes in V_{TH}.

free aromatic and non-polar ring of the BDT molecules remains exposed to the surface of the sample, increasing its hydrophobicity (see Supplementary Section 6). The network formation in BDT-functionalized MoS_2 samples improves the stability of the material in water (Fig. 2d and Supplementary Fig. 12). For MoS_2 pristine films we observe detachment and floating of the material exposed to water, whereas for MoS_2 networks the sample integrity is preserved. The solvation process is hindered within the MoS_2 network (less soluble than isolated free single flakes), consistent with the covalent interconnectivity promoted by dithiolated linkers. Such a feature is of primary importance for the fabrication of robust devices operating in an aqueous environment[2]. Additional evidence of network formation comes from the ex situ functionalization of MoS_2 flakes in solution[36,37], where the bridging process induced by the BDT linkers compromises the colloidal stability and undermines the electrical performance of the corresponding LG-TFTs (see Supplementary Section 9, Extended Data Fig. 4)[38,39]. All the above-mentioned features of the networks cannot be achieved by using monothiolated functionalizing molecules (for example, thiophenol (TP)) that are unlikely to bridge adjacent flakes (see Supplementary Section 6, Extended Data Fig. 5). Improved mechanical robustness is observed in MS_2 networks deposited on flexible substrates and subjected to multiple (5,000–10,000) deformations, highlighting another advantageous effect of the covalent bridging (see Supplementary Section 6, Supplementary Fig. 13, Extended Data Fig. 6).

LG-TFTs based on MS_2 films and networks

The covalent bridging of individual MS_2 flakes with π-conjugated molecules is expected to improve the electrical properties, especially electrical connectivity, where long-range electronic delocalization is advocated[27]. We thus investigate the performance of TFTs based on pristine MoS_2 films and networks. Dielectrically gated TFTs based on solution-processed TMDs show poor current switching ($I_{ON}/I_{OFF} < 10$)[40], encouraging one to focus on TFTs where the semiconductor layer is electrolytically gated by means of an ionic liquid solution (Fig. 3a), exploiting the inherent disorder and related porosity of the deposited materials. For LG-TFTs based on solution-processed TMD flakes, the liquid dielectric penetrates the internal free volume of the semiconducting material, thus gating the device volumetrically[28].

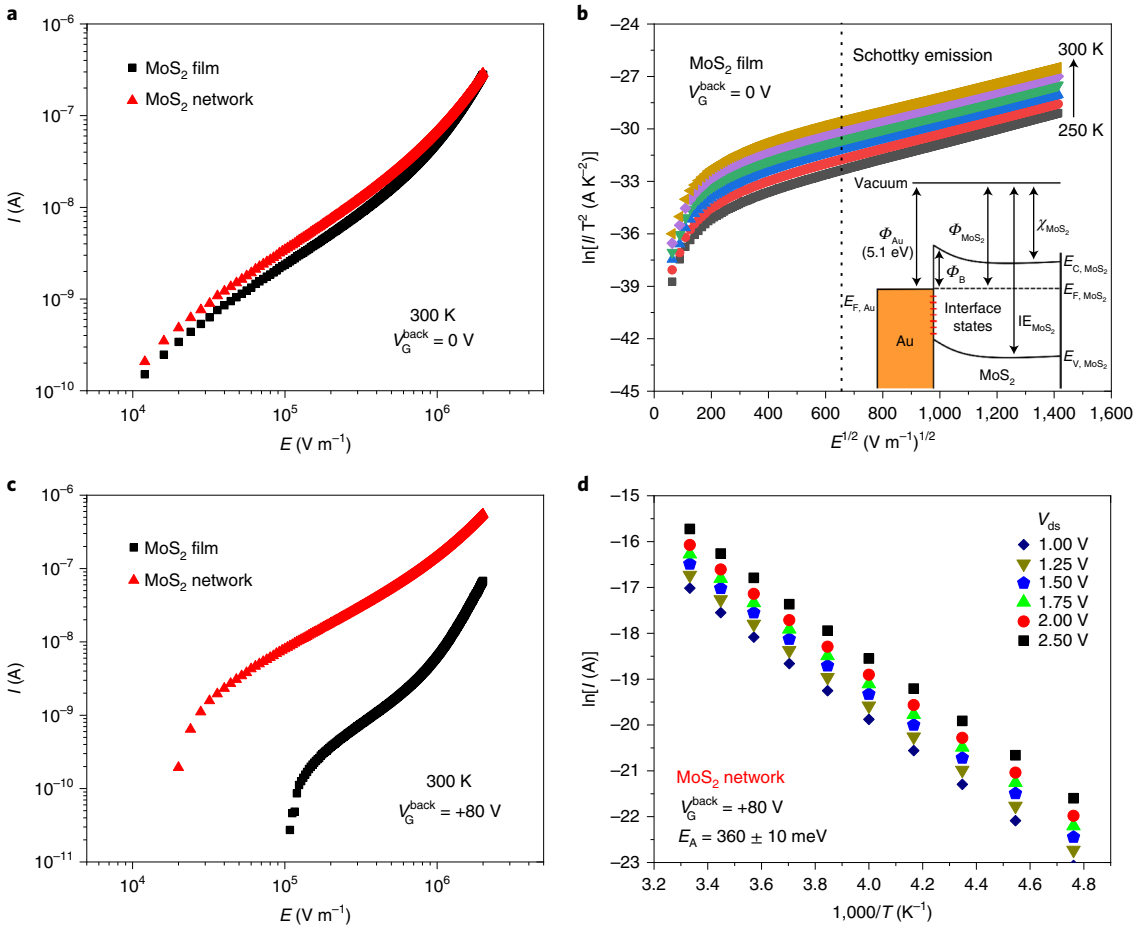

Fig. 4 | Temperature-dependent electrical characteristics. a, 300 K *I*–*E* curves with $V_G^{back} = 0$ for MoS_2 film (black) and network (red). **b**, Schottky plot for MoS_2 film with $V_G^{back} = 0$ V. Inset shows the band diagram for the Au/MoS_2 Schottky barrier interface. E_C, conduction band; E_F, Fermi level; E_V, valence band; IE, ionization energy; χ, electron affinity. **c**, 300 K *I*–*E* characteristic with $V_G^{back} = +80$ V for MoS_2 film (black) and network (red). **d**, Arrhenius plot for MoS_2 network with $V_G^{back} = +80$ V.

All our LG-TFT measurements are performed inside a glovebox under nitrogen atmosphere, to avoid side effects from environmental adsorbates, such as water and oxygen, that can induce strong p-doping[41]. Figure 3b displays the transfer curves (I_{ds} versus V_g, where I_{ds} is the source–drain current and V_g is the sweeping gate voltage) of LG-TFTs based on MoS_2 films and networks. Both show n-type transfer characteristics, with the latter featuring an overall superior performance. In particular, MoS_2 networks exhibit higher μ_{FE} up to $10^{-2}\,cm^2\,V^{-1}\,s^{-1}$ and I_{ON}/I_{OFF} up to 10^4, one order of magnitude greater than for pristine MoS_2 films (see Supplementary Section 7 for the calculation of the device figures of merit and related statistical analysis). No considerable differences in threshold voltage (V_{TH}) are observed upon bridging of flakes, proving that BDT linkers mainly affect the conductivity of the networks in terms of μ_{FE} and not the charge-carrier density (doping effect)[42].

Likewise, while applying a step-like V_g stimulus and measuring the device's time-dependent current response, a similar outcome is observed for the switching time (τ_S) of LG-TFTs based on MoS_2 films and networks. Here, τ_S is ~170 ms for a MoS_2 film and ~18 ms for a network (Fig. 3c), meaning that covalently interconnected systems result in devices that are faster by one order of magnitude, with a state-of-the-art switching performance for transistors of this kind[28]. The electrical characteristics and LG-TFT figures of merit of other solution-processed TMDs are shown in Supplementary Section 7. The reproducible tenfold enhancement of device performance observed for MS_2 networks supports the presence of covalent interconnections facilitated by π-conjugated and dithiolated linkers (Table 1), unachievable for monothiolated TP molecules that do not allow network formation (Supplementary Fig. 20). The bridging process of adjacent flakes obtained with aliphatic dithiolated molecules barely improves the electrical characteristics of MoS_2 LG-TFTs, whose performance cannot rival those achieved with BDT π-conjugated linkers (Supplementary Fig. 22, Extended Data Fig. 7).

Temperature-dependent electrical characteristics

MoS_2 films and networks are then analysed by measuring their current versus electric field (*I*–*E*) characteristics as a function of temperature (*T*) at high vacuum (10^{-6} Torr). The samples are prepared on SiO_2/Si substrates with gold IDEs. The average *E* is calculated from $V = E \times d$, where *V* is the applied bias voltage and *d* is the IDE channel distance (2.5 µm). The *I*–*E* relations are used with equations describing charge-transport models[43]. The charge-transport characteristics are measured with and without a back-gate voltage (V_G^{back}) on the n^{++}-Si substrate. At room temperature, and with $V_G^{back} = 0$, minor differences are found between the *I*–*E* traces of MoS_2 films and networks (Fig. 4a). For *T* ranging from 250 to 300 K, the current characteristics indicate Schottky emission as the dominant charge-transport mechanism (Fig. 4b). The formation of a Schottky barrier (Fig. 4b inset) with height of Φ_B at the metal/MoS_2 interface was previously investigated[44]. From the thermionic emission formalism (Supplementary Equation (4))[43], we estimate Au/MoS_2 $\Phi_B = 366 \pm 1$ meV for MoS_2 pristine films, $\Phi_B = 285 \pm 7$ meV

for MoS_2 networks and $\Phi_B = 288 \pm 16$ meV for TP-functionalized MoS_2 (Supplementary Figs. 24 and 25). Such a reduction of Φ_B upon thiol functionalization (with both BDT and TP) points to either a modification of the Au work function (Φ_{WF}) and/or healing of the Au/MoS_2 interface states[45]. Measurements of Φ_{WF} for Au electrode surfaces by photoelectron spectroscopy in air, before and after thiol treatment, reveal a small decrease from 5.11 ± 0.02 eV (bare Au) to 4.97 ± 0.10 eV and 4.93 ± 0.07 eV for BDT and TP, respectively (Supplementary Table 6). Such a small Φ_{WF} change is consistent with the passivation of Au/MoS_2 interfaces states–due to the healing of sulfur vacancies in the material–as the main cause of Φ_B reduction in thiol-functionalized samples[45]. Such a small Φ_{WF} reduction, as well as similar values found for BDT- and TP-functionalized samples, cannot explain the enhanced device performance exhibited by MoS_2 networks in LG-TFTs.

As for LG-TFTs (Fig. 3), the superior electrical performance of MoS_2 networks arises when the Schottky barrier is attenuated by the application of a sweeping gate voltage, V_g (ref. [46]). Figure 4c plots the room-temperature I–E characteristics of samples under high $V_G^{back} = +80$ V. An approximate tenfold current difference is observed for MoS_2 networks when compared with films, especially at intermediate fields ($E = 10^5$–10^6 V m^{-1}), a condition that mimics the LG-TFT operating parameters ($E \approx 10^5$ V m^{-1}). For $T = 250$–300 K and $E = 1$ MV m^{-1}, MoS_2 films and networks have a thermally activated current response (Fig. 4d and Supplementary Fig. 26) with noticeably different activation energies (E_A), ~512 ± 12 and 360 ± 10 meV, respectively (Extended Data Fig. 8). Activation energies of hundreds of meV reflect the energy necessary to overcome the inter-flake barriers in MoS_2 systems[26], rather than low-energy (tens of meV) intra-flake conduction states[26]. By sweeping V_G^{back} from −60 to +60 V, the temperature-dependent charge-carrier mobility $\mu(T)$ of films and networks follows an Arrhenius relation, with lower E_A for networks (Supplementary Fig. 27). Hence, as inter-flake processes appear to be the limiting factor for charge transport within TMD thin films[41], a reduced E_A points to a reduction in inter-flake junction resistance, which would be consistent with the observed mobility increase upon network formation. The activation energies for TP-functionalized samples (500 ± 1 meV) are only slightly smaller than the values found for pristine MoS_2 films, revealing a reduction of trap states caused by the sulfur-vacancy healing mechanism, without any further improvement due to the inter-flake connectivity (see Supplementary Section 8).

Conclusions

We reported a universal and simple route for the production of covalently interconnected TMD networks by exploiting defect engineering in solution-processed layered materials. We used π-conjugated dithiolated molecules to bridge adjacent MS_2 flakes, forming networks characterized by substantially different physicochemical properties (improved electrical characteristics, water stability and mechanical robustness). The bridging of neighbouring flakes at the molecular level improves the charge transport across the network, thereby leading to superior device performances. LG-TFTs show a reproducible increase by one order of magnitude in the main figures of merit, leading to a state-of-the-art field-effect mobility (~10^{-2} cm^2 V^{-1} s^{-1}) and I_{ON}/I_{OFF} (~10^4), along with the fastest switching time (~18 ms) reported for devices of this kind[28,47]. Our findings pave the way for the development of high-performance, large-area and printed electronics based on solution-processed TMDs. The network formation results in water-stable and mechanically robust MS_2-based devices that could be exploited in (bio)sensing[48], (photo)catalysis[2] and flexible optoelectronics[49]. Ultimately, with an appropriate molecular design of the bridging linkers, one might endow the TMD networks with diverse functionalities, tuning the final properties *on demand* according to their final applications.

Online content

Any methods, additional references, Nature Research reporting summaries, source data, extended data, supplementary information, acknowledgements, peer review information; details of author contributions and competing interests; and statements of data and code availability are available at https://doi.org/10.1038/s41565-021-00857-9.

Received: 8 February 2020; Accepted: 15 January 2021;
Published online: 25 February 2021

References

1. Wang, Q. H., Kalantar-Zadeh, K., Kis, A., Coleman, J. N. & Strano, M. S. Elec0tronics and optoelectronics of two-dimensional transition metal dichalcogenides. *Nat. Nanotechnol.* **7**, 699–712 (2012).
2. Voiry, D., Yang, J. & Chhowalla, M. Recent strategies for improving the catalytic activity of 2D TMD nanosheets toward the hydrogen evolution reaction. *Adv. Mater.* **28**, 6197–6206 (2016).
3. Chen, Y., Tan, C., Zhang, H. & Wang, L. Two-dimensional graphene analogues for biomedical applications. *Chem. Soc. Rev.* **44**, 2681–2701 (2015).
4. Ferrari, A. C. et al. Science and technology roadmap for graphene, related two-dimensional crystals, and hybrid systems. *Nanoscale* **7**, 4598–4810 (2015).
5. Manzeli, S., Ovchinnikov, D., Pasquier, D., Yazyev, O. V. & Kis, A. 2D transition metal dichalcogenides. *Nat. Rev. Mater.* **2**, 17033 (2017).
6. Han, J. H., Kwak, M., Kim, Y. & Cheon, J. Recent advances in the solution-based preparation of two-dimensional layered transition metal chalcogenide nanostructures. *Chem. Rev.* **118**, 6151–6188 (2018).
7. Backes, C. et al. Production and processing of graphene and related materials. *2D Mater.* **7**, 022001 (2020).
8. O'Neill, A., Khan, U. & Coleman, J. N. Preparation of high concentration dispersions of exfoliated MoS_2 with increased flake size. *Chem. Mater.* **24**, 2414–2421 (2012).
9. Yao, Y. et al. High-concentration aqueous dispersions of MoS_2. *Adv. Funct. Mater.* **23**, 3577–3583 (2013).
10. Bonaccorso, F., Bartolotta, A., Coleman, J. N. & Backes, C. 2D-crystal-based functional inks. *Adv. Mater.* **28**, 6136–6166 (2016).
11. Bonaccorso, F. et al. Production and processing of graphene and 2d crystals. *Mater. Today* **15**, 564–589 (2012).
12. Raccichini, R., Varzi, A., Passerini, S. & Scrosati, B. The role of graphene for electrochemical energy storage. *Nat. Mater.* **14**, 271–279 (2015).
13. Jariwala, D., Sangwan, V. K., Lauhon, L. J., Marks, T. J. & Hersam, M. C. Emerging device applications for semiconducting two-dimensional transition metal dichalcogenides. *ACS Nano* **8**, 1102–1120 (2014).
14. Ciesielski, A. & Samorì, P. Graphene via sonication assisted liquid-phase exfoliation. *Chem. Soc. Rev.* **43**, 381–398 (2014).
15. Backes, C. et al. Equipartition of energy defines the size–thickness relationship in liquid-exfoliated nanosheets. *ACS Nano* **13**, 7050–7061 (2019).
16. Tsai, C. et al. Electrochemical generation of sulfur vacancies in the basal plane of MoS_2 for hydrogen evolution. *Nat. Commun.* **8**, 15113 (2017).
17. Komsa, H.-P. et al. Two-dimensional transition metal dichalcogenides under electron irradiation: defect production and doping. *Phys. Rev. Lett.* **109**, 035503 (2012).
18. McDonnell, S., Addou, R., Buie, C., Wallace, R. M. & Hinkle, C. L. Defect-dominated doping and contact resistance in MoS_2. *ACS Nano* **8**, 2880–2888 (2014).
19. Nicolosi, V., Chhowalla, M., Kanatzidis, M. G., Strano, M. S. & Coleman, J. N. Liquid exfoliation of layered materials. *Science* **340**, 1226419 (2013).
20. Voiry, D. et al. Covalent functionalization of monolayered transition metal dichalcogenides by phase engineering. *Nat. Chem.* **7**, 45–49 (2015).
21. Ippolito, S., Ciesielski, A. & Samorì, P. Tailoring the physicochemical properties of solution-processed transition metal dichalcogenides via molecular approaches. *Chem. Commun.* **55**, 8900–8914 (2019).
22. Bertolazzi, S., Gobbi, M., Zhao, Y., Backes, C. & Samorì, P. Molecular chemistry approaches for tuning the properties of two-dimensional transition metal dichalcogenides. *Chem. Soc. Rev.* **47**, 6845–6888 (2018).
23. Schmidt, H., Giustiniano, F. & Eda, G. Electronic transport properties of transition metal dichalcogenide field-effect devices: surface and interface effects. *Chem. Soc. Rev.* **44**, 7715–7736 (2015).
24. Sim, D. M. et al. Controlled doping of vacancy-containing few-layer MoS_2 via highly stable thiol-based molecular chemisorption. *ACS Nano* **9**, 12115–12123 (2015).
25. Yu, X., Prévot, M. S. & Sivula, K. Multiflake thin film electronic devices of solution processed 2D MoS_2 enabled by sonopolymer assisted exfoliation and surface modification. *Chem. Mater.* **26**, 5892–5899 (2014).
26. Zeng, X., Hirwa, H., Metel, S., Nicolosi, V. & Wagner, V. Solution processed thin film transistor from liquid phase exfoliated MoS_2 flakes. *Solid State Electron.* **141**, 58–64 (2018).

27. Noriega, R. et al. A general relationship between disorder, aggregation and charge transport in conjugated polymers. *Nat. Mater.* **12**, 1038–1044 (2013).
28. Kelly, A. G. et al. All-printed thin-film transistors from networks of liquid-exfoliated nanosheets. *Science* **356**, 69–73 (2017).
29. Schilter, D. Thiol oxidation: a slippery slope. *Nat. Rev. Chem.* **1**, 0013 (2017).
30. Donarelli, M., Bisti, F., Perrozzi, F. & Ottaviano, L. Tunable sulfur desorption in exfoliated MoS_2 by means of thermal annealing in ultra-high vacuum. *Chem. Phys. Lett.* **588**, 198–202 (2013).
31. McIntyre, N. S., Spevack, P. A., Beamson, G. & Briggs, D. Effects of argon ion bombardment on basal plane and polycrystalline MoS_2. *Surf. Sci.* **237**, L390–L397 (1990).
32. Mignuzzi, S. et al. Effect of disorder on Raman scattering of single-layer MoS_2. *Phys. Rev. B* **91**, 195411 (2015).
33. Bae, S. et al. Defect-induced vibration modes of Ar^+-irradiated MoS_2. *Phys. Rev. Appl.* **7**, 024001 (2017).
34. Park, S. Y. et al. Highly selective and sensitive chemoresistive humidity sensors based on rGO/MoS_2 van der Waals composites. *J. Mater. Chem. A* **6**, 5016–5024 (2018).
35. Chow, P. K. et al. Wetting of mono and few-layered WS_2 and MoS_2 films supported on Si/SiO_2 substrates. *ACS Nano* **9**, 3023–3031 (2015).
36. Nguyen, E. P. et al. Electronic tuning of 2D MoS_2 through surface functionalization. *Adv. Mater.* **27**, 6225–6229 (2015).
37. Chou, S. S. et al. Ligand conjugation of chemically exfoliated MoS_2. *J. Am. Chem. Soc.* **135**, 4584–4587 (2013).
38. Kim, J. et al. Direct exfoliation and dispersion of two-dimensional materials in pure water via temperature control. *Nat. Commun.* **6**, 8294 (2015).
39. Graetzel, M., Janssen, R. A. J., Mitzi, D. B. & Sargent, E. H. Materials interface engineering for solution-processed photovoltaics. *Nature* **488**, 304–312 (2012).
40. Li, J., Naiini, M. M., Vaziri, S., Lemme, M. C. & Östling, M. Inkjet printing of MoS_2. *Adv. Funct. Mater.* **24**, 6524–6531 (2014).
41. Li, S.-L., Tsukagoshi, K., Orgiu, E. & Samorì, P. Charge transport and mobility engineering in two-dimensional transition metal chalcogenide semiconductors. *Chem. Soc. Rev.* **45**, 118–151 (2015).
42. Wang, Y., Gali, S. M., Slassi, A., Beljonne, D. & Samorì, P. Collective dipole-dominated doping of monolayer MoS_2: orientation and magnitude control via the supramolecular approach. *Adv. Funct. Mater.* **30**, 2002846 (2020).
43. Chiu, F.-C. A review on conduction mechanisms in dielectric films. *Adv. Mater. Sci. Eng.* **2014**, 578168 (2014).
44. Lee, K. et al. Electrical characteristics of molybdenum disulfide flakes produced by liquid exfoliation. *Adv. Mater.* **23**, 4178–4182 (2011).
45. Sze, S. M. & Ng, K. K. *Physics of Semiconductor Devices* (John Wiley & Sons, 2006).
46. Vladimirov, I. et al. Bulk transport and contact limitation of MoS_2 multilayer flake transistors untangled via temperature-dependent transport measurements. *Physica Status Solidi A* **212**, 2059–2067 (2015).
47. Higgins, T. M. et al. Electrolyte-gated n-type transistors produced from aqueous inks of WS_2 nanosheets. *Adv. Funct. Mater.* **29**, 1804387 (2019).
48. Anichini, C. et al. Chemical sensing with 2D materials. *Chem. Soc. Rev.* **47**, 4860–4908 (2018).
49. Akinwande, D., Petrone, N. & Hone, J. Two-dimensional flexible nanoelectronics. *Nat. Commun.* **5**, 5678 (2014).

Methods

Device preparation. Bottom-contact SiO_2/n^{++}-Si substrates (15 × 15 mm; Fraunhofer IPMS) are used. They consist of thermally grown SiO_2 (230 nm thick) having IDEs (30-nm-thick gold on a 10 nm indium tin oxide adhesion layer) spaced at 2.5 µm, yielding a channel width:length ratio of ~4,000. Before use, the substrates are cleaned by ultrasonication in acetone and 2-propanol (10 min each) and dried under nitrogen flow afterwards.

The films are moved in a nitrogen-filled glovebox for the following functionalization steps: (1) sample immersion in a 50 mM saturated solution of BDT in anhydrous hexane for 24 h inside a sealed container, (2) spin-rinsing with anhydrous hexane (5 ml, 4,000 r.p.m., acceleration 4,000 r.p.m. per second, 60 s) and (3) annealing at 90 °C for 30–45 min.

Electrical characterization. The LG-TFT performances are evaluated by their transfer characteristics (I_{ds} versus V_g), using a platinum wire as the gate electrode and a droplet of 1-ethyl-3-methylimidazolium bis(trifluoromethylsulfonyl) imide (EMI-TFSI) as the ionic liquid gate dielectric. The source–drain current (I_{ds}) is recorded while sweeping the gate voltage (V_g) from −2.5 to +2.5 V, at a source–drain voltage $V_{ds} = -0.1$ V. The current–electric field traces (I_{ds}–E) are measured for $T = 80$–300 K, using an Oxford Instruments Optistat DN-V cryostat, for $V_G^{back} = 0$ and +80 V. All electrical measurements are carried out in the dark and under a nitrogen atmosphere using a Keithley 2636 A SourceMeter unit. To enable statistical analysis, ~60 identical devices are produced and subjected to the different electrical characterizations.

Further details about the materials, characterization techniques and data treatment can be found in the Supplementary Information.

Data availability

Source data are provided with this paper. The data that support the findings of this study are available from the corresponding author upon reasonable request.

Acknowledgements

We acknowledge funding from the European Commission through the Graphene Flagship, the ERC Grants SUPRA2DMAT (GA-833707), FUTURE-PRINT (GA-694101), Hetero2D and GSYNCOR, the EU Grant Neurofibres, the Agence Nationale de la Recherche through the Labex projects CSC (ANR-10-LABX-0026 CSC) and NIE (ANR-11-LABX-0058 NIE) within the Investissement d'Avenir programme (ANR-10-120 IDEX-0002-02), the International Center for Frontier Research in Chemistry (icFRC), EPSRC Grants EP/K01711X/1, EP/K017144/1, EP/N010345/1 and EP/L016057/1, and the Faraday Institution. The HAADF-STEM characterization was carried out at the Advanced Microscopy Laboratory (Dublin), a Science Foundation Ireland (SFI) supported centre.

Author contributions

S.I. and P.S. conceived the experiments and designed the study. A.G.K., Z.B., L.L., Y.A.S., A.C.F. and J.N.C. produced the raw materials and characterized them by spectroscopic and electrochemical techniques. S.I. designed and performed the multiscale characterizations on the final functionalized materials. R.F.O. and M.-A.S. designed and performed the charge-carrier transport measurements and studies. D.I. carried out the NMR measurements and analysis. A.R., C.D. and V.N. designed and performed the HAADF-STEM investigations. All authors discussed the results and contributed to the interpretation of data. S.I., R.F.O. and P.S. co-wrote the paper with input from all co-authors.

Competing interests

The authors declare no competing interests.

Additional information

Extended data is available for this paper at https://doi.org/10.1038/s41565-021-00857-9.

Supplementary information The online version contains supplementary material available at https://doi.org/10.1038/s41565-021-00857-9.

Correspondence and requests for materials should be addressed to P.S.

Peer review information *Nature Nanotechnology* thanks Damien Voiry and the other, anonymous, reviewer(s) for their contribution to the peer review of this work.

Reprints and permissions information is available at www.nature.com/reprints.

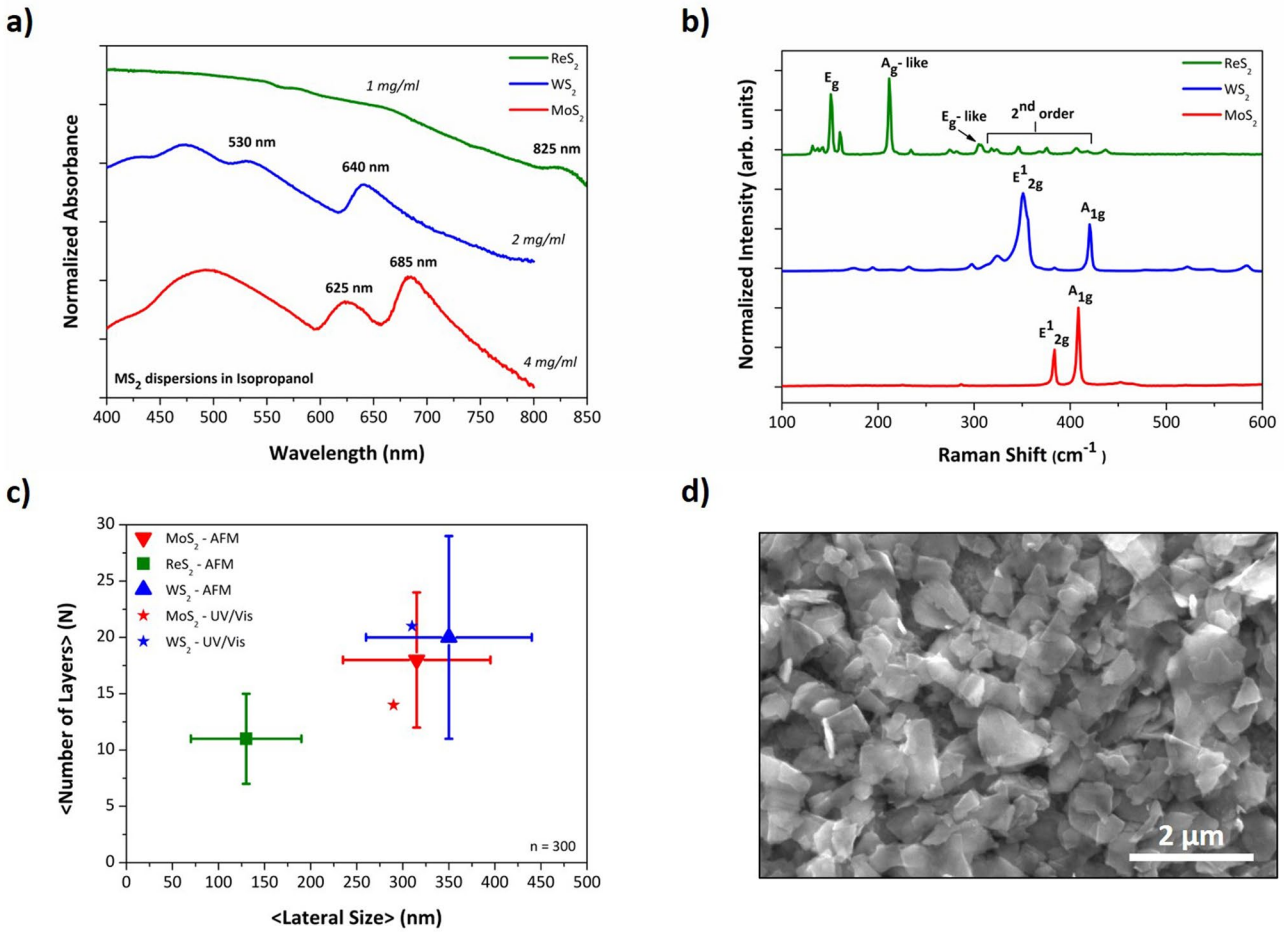

Extended Data Fig. 1 | Spectroscopic and morphological characterization of solution-processed MS_2. a, UV-Vis spectra (solution). **b**, Raman spectra (film). **c**, Statistical AFM analysis performed on 300 individual MS_2 flakes and comparison with values estimated *via* UV-Vis spectroscopy. **d**, Typical SEM image of drop-cast MoS_2 flakes.

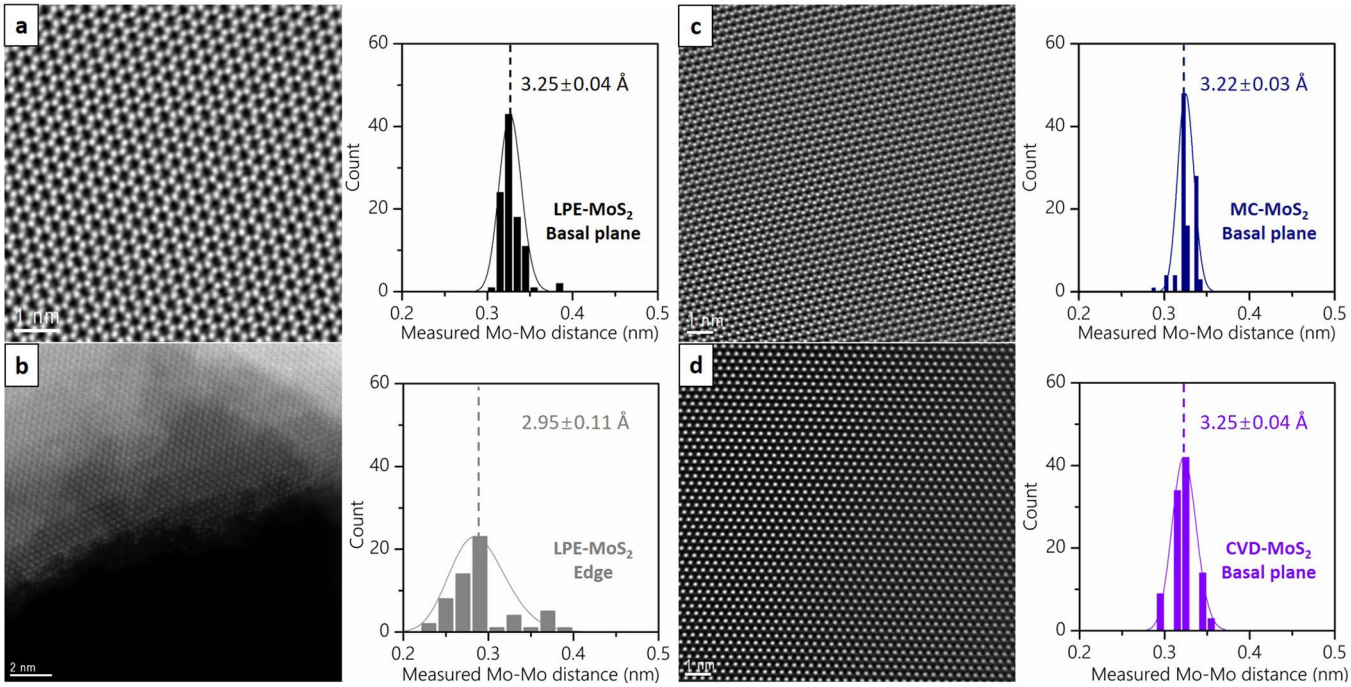

Extended Data Fig. 2 | HAADF-STEM investigation. HAADF-STEM images and related histograms of Mo-Mo distance for the **a**, basal plane of LPE-MoS_2, **b**, edge of LPE-MoS_2, **c**, basal plane of MC-MoS_2 and **d**, basal plane of CVD-MoS_2. The histograms show a similar average Mo-Mo distance for the basal plane of all samples, with a significant decrease ~30 pm for the edge of LPE-MoS_2, pointing to a higher defect density.

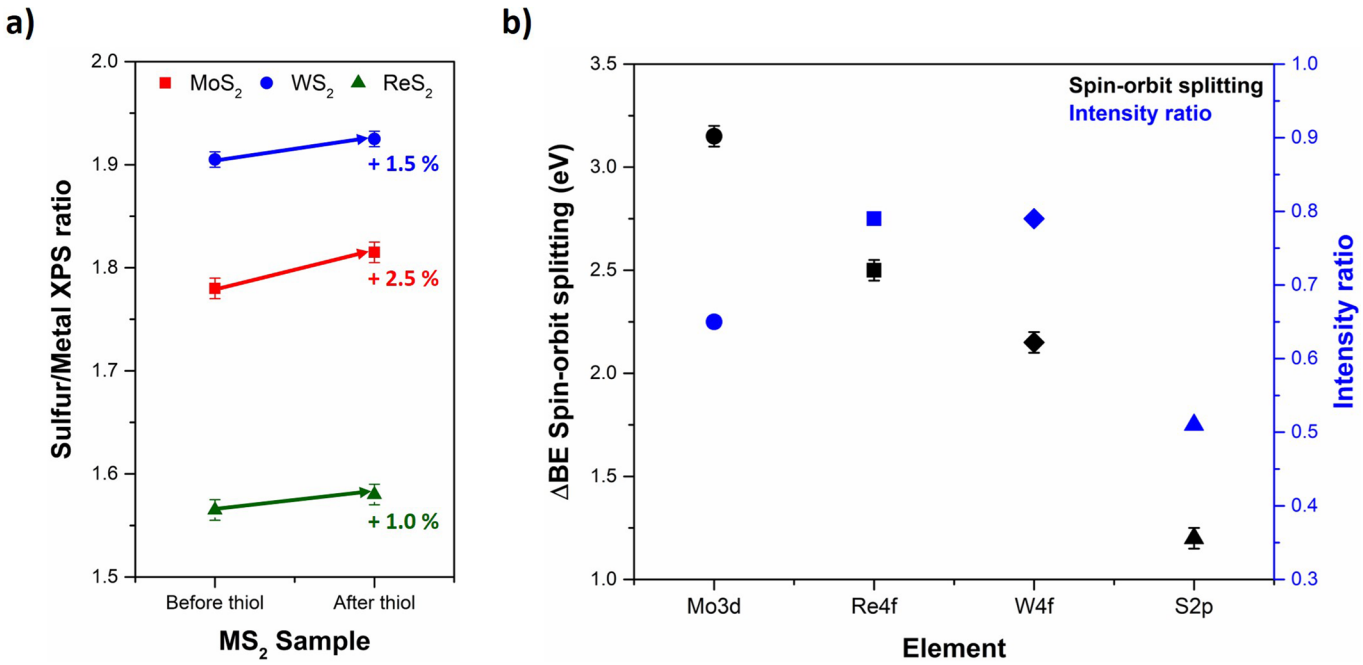

Extended Data Fig. 3 | XPS analysis. a, Sulfur/Metal XPS ratio before and after exposure to BDT molecules for MoS_2, WS_2 and ReS_2. **b**, Summary of the XPS constraints (spin-orbit splitting and intensity ratio) implemented for the fitting of Mo3d, Re4f, W4f and S2p regions, before and after exposure to BDT molecules.

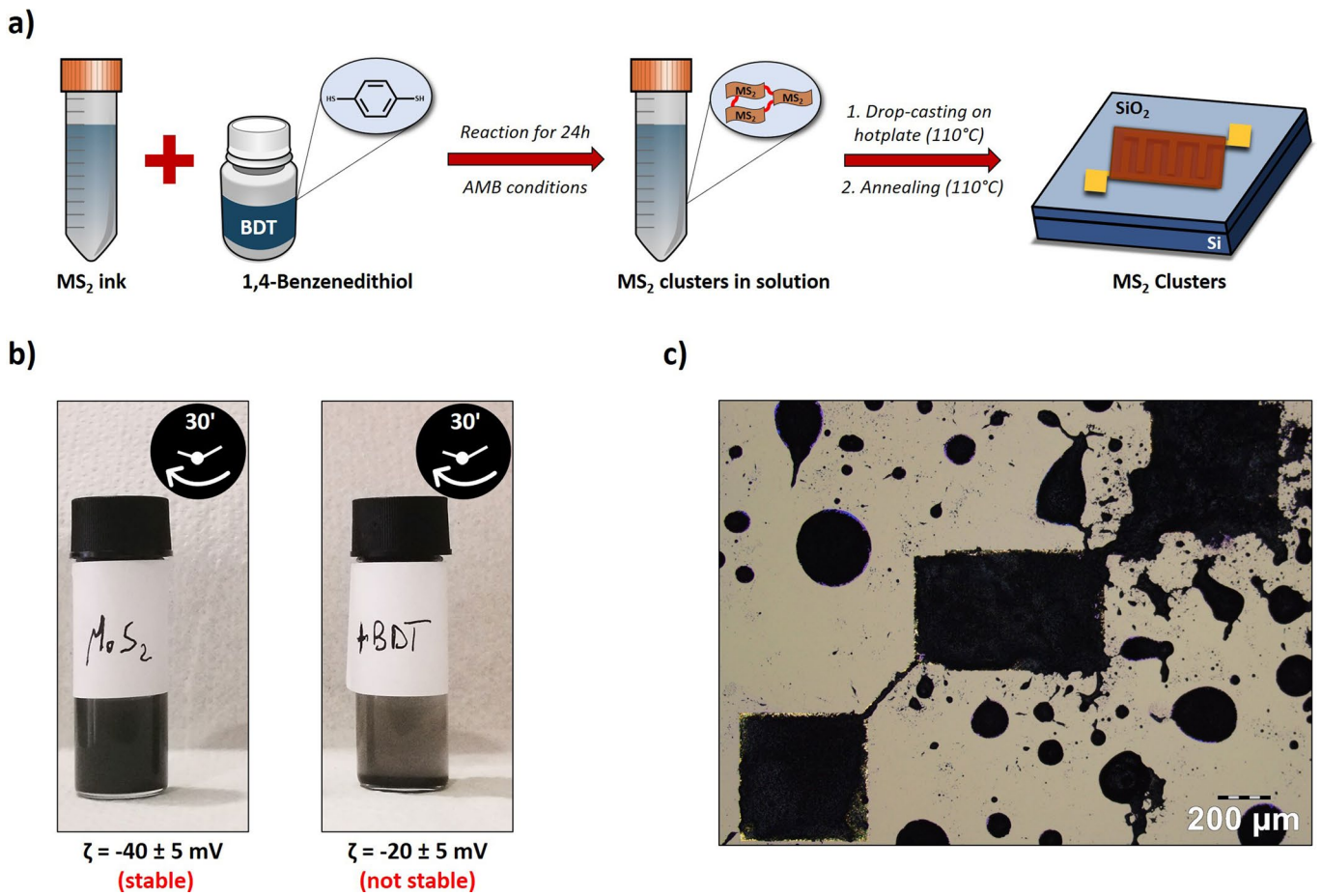

Extended Data Fig. 4 | Ex-situ functionalization with BDT. a, Schematic illustration for the *ex-situ* functionalization of MS_2 inks with BDT. **b**, Outcome of stability test for pristine and BDT-functionalized MoS_2 ink, along with the related zeta potential values. **c**, Optical image of a IDE device covered with BDT-functionalized MoS_2 ink *via ex-situ* approach.

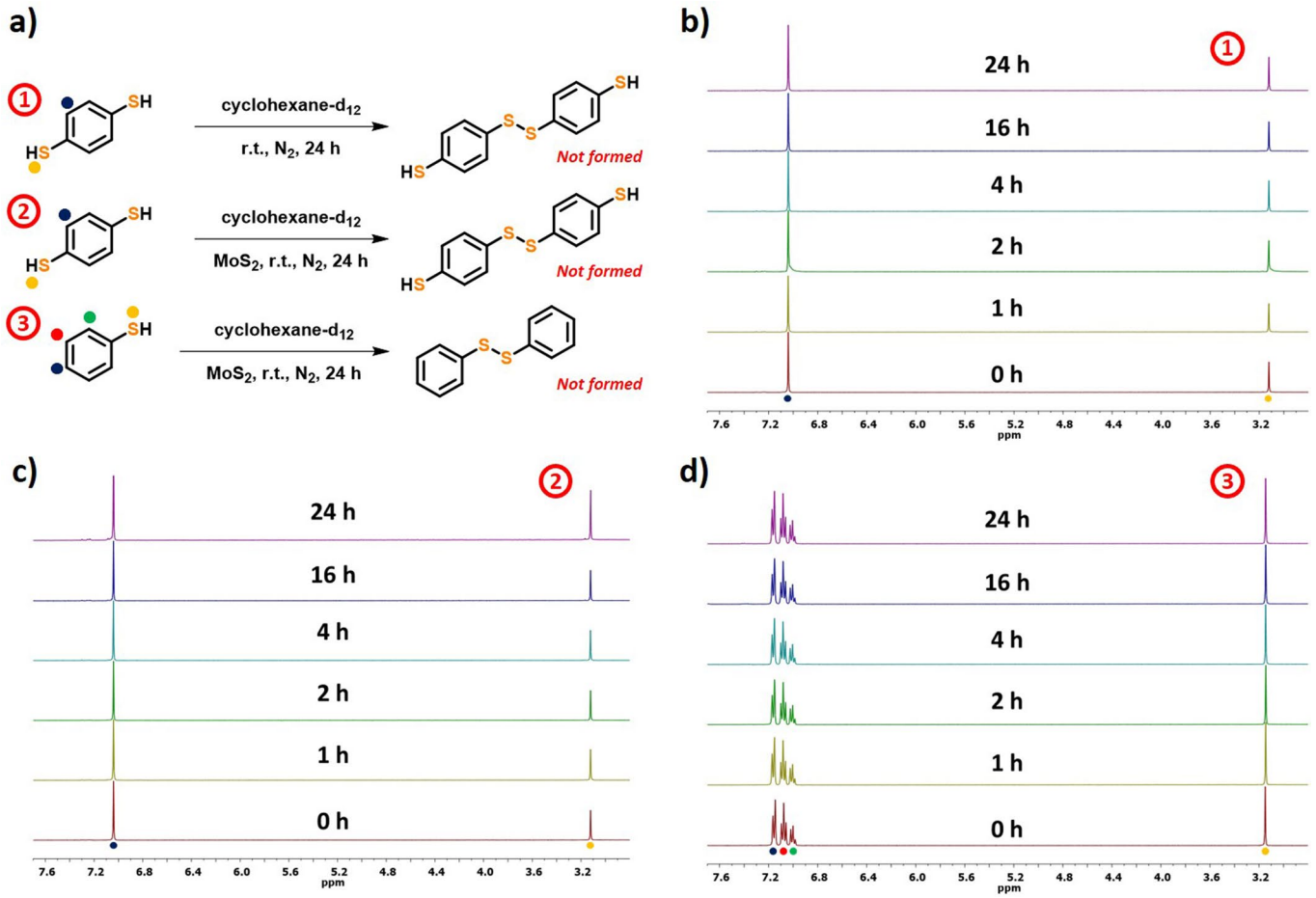

Extended Data Fig. 5 | NMR investigation. a, Tested reactions between MoS_2 and thiolated molecules under exam (TP and BDT). Related NMR spectra at different time intervals for **b**, control experiment (BDT without MoS_2), **c**, MoS_2 + BDT and **d**, MoS_2 + TP.

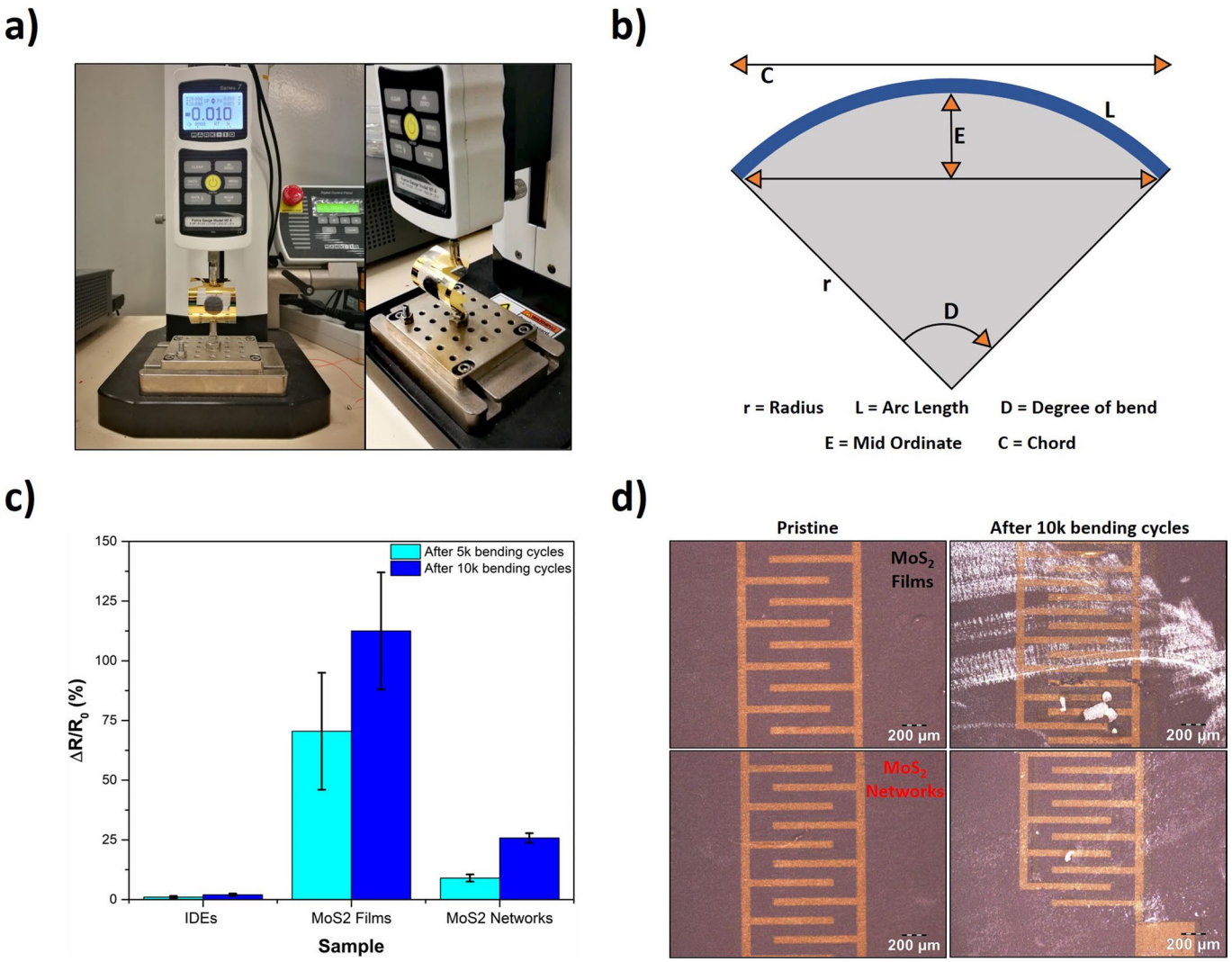

Extended Data Fig. 6 | Mechanical test. a, Experimental setup. **b**, Sketch of the samples subjected to bending deformation. **c**, Variation of the relative channel resistance $\Delta R/R_0$ of bare IDEs, MoS_2 films, and MoS_2 networks upon 5k and 10k bending cycles, along with related **d**, optical images of MoS_2 films and networks before (left) and after (right) mechanical deformation.

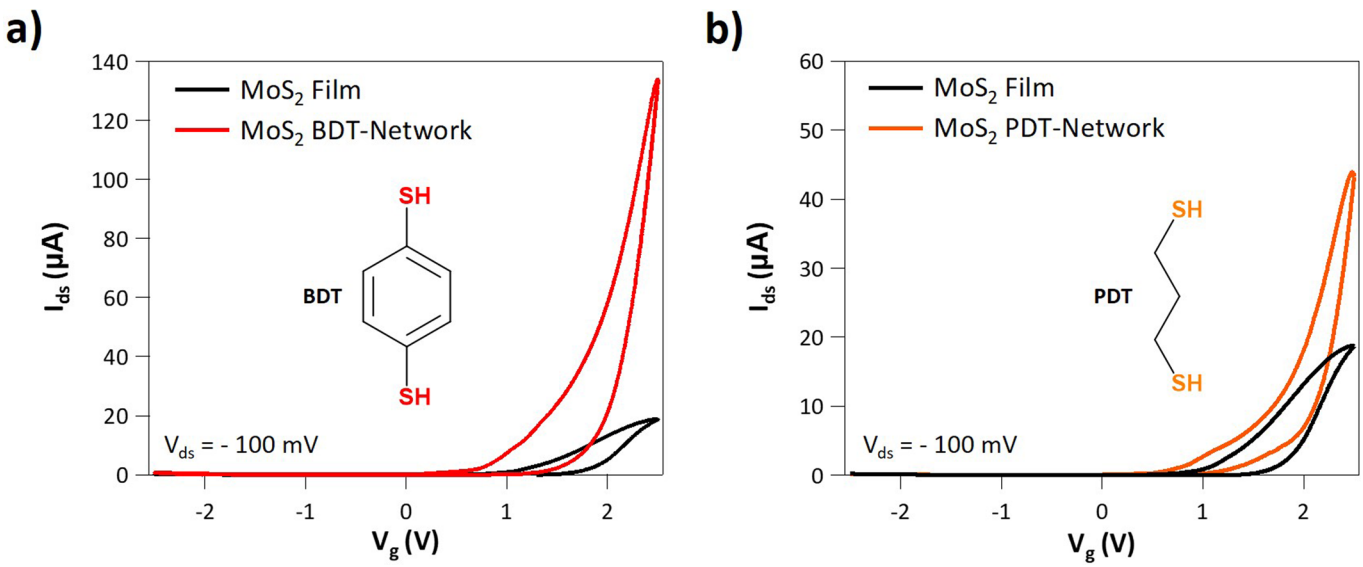

Extended Data Fig. 7 | Influence of the linker structure on electrical performance of MoS_2 networks. Transfer curves for MoS_2 LG-TFTs **a**, before and after treatment with BDT linkers and **b**, before and after treatment with PDT linkers. All curves are recorded at V_{ds} = -100 mV, using EMI-TFSI as electrolyte and a Pt wire as gate electrode. The molecular structures of BDT and PDT are also indicated.

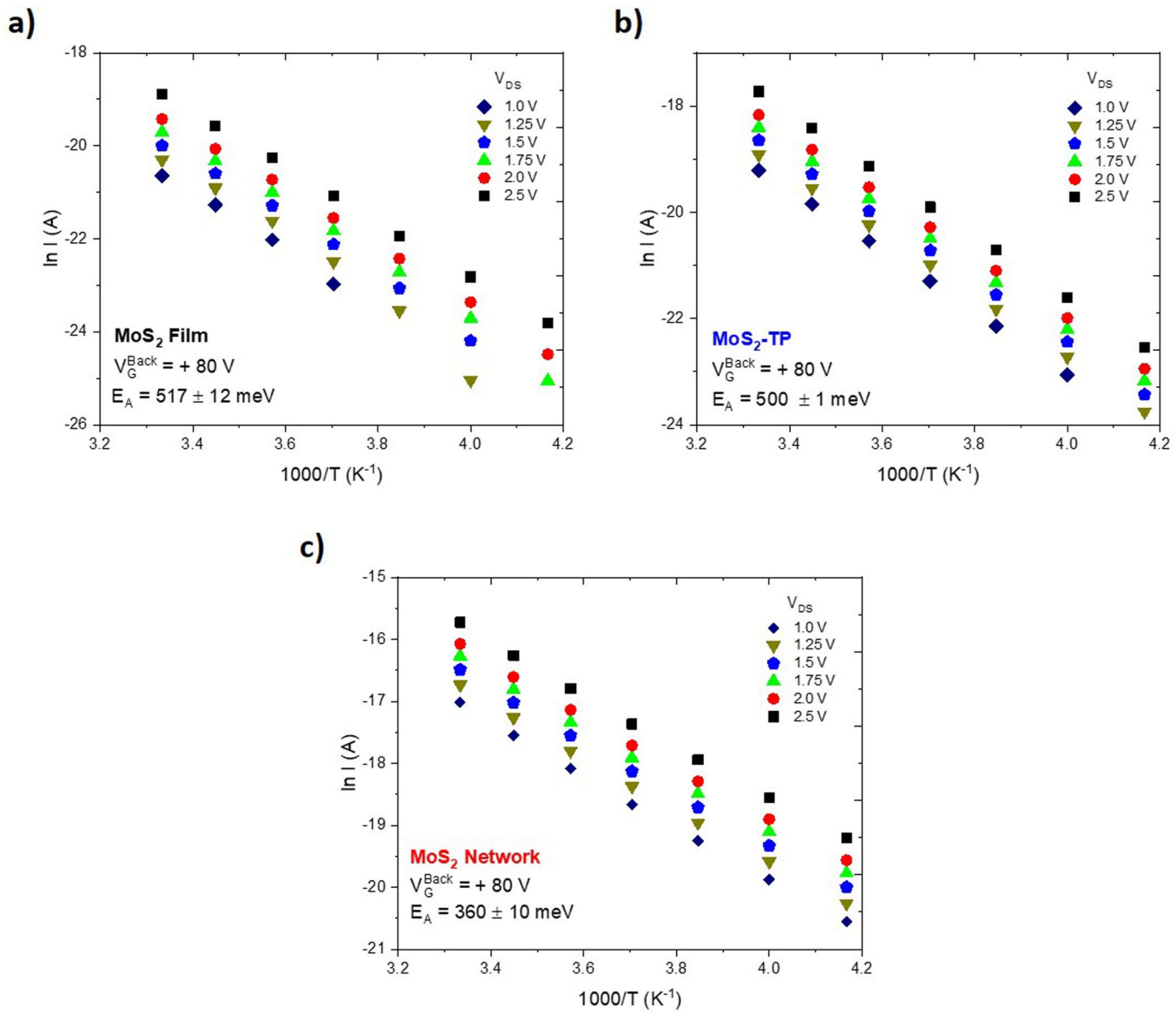

Extended Data Fig. 8 | Thermally-activated current response. Ln I *vs.* 1000/T for V_G^{back} = + 80 V in **a**, MoS_2 films **b**, TP-functionalized samples and **c**, MoS_2 networks. E_A is calculated from the curve slope with errors associated to different applied bias on the IDEs (from 1-2.5 V, *that is*, $E = 4 \times 10^5 - 1 \times 10^6$ V/m).